Supporting Information

A Low-Cost Solution to the Grid Reliability Problem With 100% Penetration of Intermittent Wind, Water, and Solar for all Purposes

Mark Z. Jacobson, Mark A. Delucchi, Mary A. Cameron, Bethany A. Frew

Proceedings of the National Academy of Sciences, 112, doi:10.1073/pnas.1510028112, 2015

SI Text

S1. Materials and Methods

For this study, the GATOR-GCMOM (Gas, Aerosol, Transport, Radiation, General Circulation, Mesoscale, and Ocean Model) global-through-local climate-pollution-weather-forecast model (1-3) is used to simulate the time- and space-dependent power extraction by wind turbines, rooftop solar PV panels, utility-scale solar PV power plants, and CSP power plants under a 2050 scenario where 100% of all-purpose energy in each of the 48 continental United States is derived from wind, water, and sunlight (WWS) for all purposes. The 2050 100% WWS state-by-state roadmaps and their derivations are provided in (4).

GATOR-GCMOM simulates feedbacks among meteorology, radiation, gases, aerosol particles, cloud hydrometeor particles, oceans, sea ice, snow, soil, vegetation, and radiation. The model extracts the correct amount of energy from the wind at different model heights intersecting each wind turbine rotor blade based on the turbine power curve, as described in Section S1.H and in (2, 3). It also accounts for feedback of wind speed changes to energy and moisture fluxes at the surface and extraction of solar radiation by solar devices (Section S1.I). Below, the model is briefly described.

S1.A. Atmospheric Meteorology and Transport

The momentum, thermodynamic energy, and continuity equations are solved for the atmosphere with a potential-enstrophy, vorticity, energy, and mass-conserving scheme (5). Winds and turbulence predicted by the model drive the horizontal and vertical transport of gases and size- and composition-resolved aerosol particles with a monotonic advection scheme (6). Subgrid turbulent kinetic energy is calculated as a function of instantaneous modeled grid-scale wind shear and buoyancy as well as shear due to wind turbines themselves.

S1.B. Subgrid Ocean, Sea Ice, Land, Vegetation, and Snow Surfaces

The model treats 17 subgrid surface classes in each surface grid cell and energy and vapor exchange between the atmosphere and each subgrid surface in each cell. The surface classes include 13 soil classes, water bodies, roads, roofs, and deep snow/ice (7). Sea ice can form on top of water, and snow can deposit on sea ice and land (1, 8). Within each land grid cell, soil temperatures and moisture are calculated over time separately for each subgrid soil class in each of 10 subsurface soil layers with top-to-bottom layer thicknesses of 0.005, 0.01,

0.01, 0.01, 0.015, 0.025, 0.05, 0.1, 5, and 5 m, respectively. Thus, subgrid, subsurface temperatures and moisture are tracked perpetually and independently throughout each simulation. The same 10-layer subsurface module is applied to permanent snow (e.g., over the Antarctic) and to roads and roofs.

On land surfaces, each subgrid soil class is divided into vegetated and bare soil. Snow can accumulate on soil and vegetation. For bare and vegetated soil, the surface energy balance equation accounts for latent heat, sensible heat, solar, thermal-IR, and conductive energy fluxes. However, for vegetated soil, the fluxes take into account the foliage temperature and moisture as well as the temperature and moisture of the air within the foliage, all of which are tracked prognostically in time or diagnostically from prognostic parameters by iteration (1). Foliage temperature and moisture are a function of evapotranspiration, which conserves water in the model. When snow is on top of vegetation or bare soil, an additional model layer with thickness equal to that of the snow is added to the 10-layer subsurface module.

Oceans in the model are represented in 3-D for some calculations and 2-D for others. A 2-D time-dependent mixed-layer ocean dynamics model driven by surface wind stress is used to solve for mixed-layer velocities, heights, and horizontal energy transport in each grid cell (8). The scheme conserves potential enstrophy, vorticity, energy, and mass and predicted gyres and major currents. Energy diffusion to the deep ocean is treated in 3-D through 10 ocean layers below each surface ocean grid cell (9). Air-ocean exchange, vertical diffusion through the ocean, and 3-D ocean equilibrium chemistry and pH are solved among the Na-Cl-Mg-Ca-K-H-O-Li-Sr-C-S-N-Br-F-B-Si-P system (9). Drag at the ocean surface is calculated as a function of 10-m wind speed (10). Sea ice in the model forms, evolves, and flows horizontally on subgrid water surfaces, and snow can accumulate on sea ice.

S1.C. Gas Processes

Gas processes include emissions, gas photochemistry, gas-to-particle conversion, gas-to-cloud conversion, gas-cloud exchange, gas-precipitation exchange, gas-ocean exchange, advection, convection, molecular diffusion, turbulent diffusion, and dry deposition. Gas photochemistry is solved with SMVGEAR II (11) for ~180 species and ~440 tropospheric and stratospheric kinetic, heterogeneous (on particle surfaces), and photolysis reactions.

S1.D. Aerosol Processes

Aerosol processes include anthropogenic and natural emissions, binary and ternary homogeneous nucleation, condensation, dissolution, internal-particle chemical equilibrium, aerosol-aerosol coagulation, aerosol activation of clouds, aerosol-hydrometeor coagulation, sedimentation, dry deposition, and transport (12, 13). Chemical equilibrium calculations included the determination of the solid/liquid/ion composition, pH, and liquid water content of aerosols as a function of size. The model treats any number of discrete aerosol size distributions, each with any number of discrete size bins and chemicals per size bin. Particle number and chemical mole concentrations are tracked in each grid cell. The components within each size bin of each aerosol size distribution are internally mixed in the bin but externally mixed from other bins and other size distributions.

S1.E. Clouds and Aerosol-Cloud Processes

Aerosol-cloud interactions and cloud/precipitation evolution in GATOR-GCMOM are treated as explicitly as possible. The model simulates the size- and composition-resolved microphysical evolution of clouds and precipitation, the first and second aerosol indirect effects, the semi-direct effect, and cloud absorption effects I and II (which are the heating of a cloud due to solar absorption by absorbing inclusions in cloud drops and by swollen absorbing aerosol particles interstitially between cloud drops, respectively). Microphysical processes are treated with discrete, size- and composition resolution for both aerosol particles and hydrometeor particles (14, 15).

For global simulations, cloud thermodynamics is parameterized to treat multiple subgrid cumulus clouds in each column based on an Arakawa-Schubert treatment as described in (15). Up to 500 convective clouds can form per grid column, each with a different base and top. Cloud and precipitation microphysics is time-dependent, explicit, and size- and composition-resolved within each subgrid cloud. Further, aerosol particles of all composition and size and all gases are convected vertically within each subgrid cloud.

S1.F. Aerosol and Hydrometeor Size Distribution, Composition, and Interactions

Three discrete (multiple size bin) aerosol size distributions and three discrete hydrometeor distributions are treated for the present simulations. The three aerosol distributions are an emitted fossil-fuel soot (EFFS) distribution, an emitted combined biofuel-soot and biomass-burning-soot (BFBB) distribution, and an ultimate internally-mixed (UIM) distribution. Each aerosol size distribution contains 14 size bins. The three hydrometeor size distributions treated are liquid, ice, and graupel, each with 30 size bins (0.5 μm to 8 mm in diameter).

Each size bin of the EFFS aerosol distribution contains black carbon (BC), weakly-to-moderately-absorbing primary organic matter (POM), secondary organic matter (SOM), hydrated liquid water, H_2SO_4(aq), HSO_4^-, SO_4^{2-}, NO_3^-, Cl^-, H^+, NH_4^+, NH_4NO_3(s), and $(NH_4)_2SO_4$(s). Each size bin of the BFBB distribution contains these same components plus tar balls (a strongly-absorbing form of brown carbon), Na^+, K^+, Ca^{2+}, and Mg^{2+}. Each size bin of the UIM distribution contains the same components as the EFFS and BFBB distributions plus soil dust, pollen, spores, and bacteria. Each size bin of each hydrometeor distribution contains the same components as in all three aerosol distributions plus condensed liquid water or deposited ice.

Gases, such as HNO_3, HCl, NH_3, H_2SO_4, and organics condense onto or dissolve into EFFS, BFBB, and IM particles and dissolve within liquid hydrometeor particles or react on ice and graupel particle surfaces. During coagulation, the chemical components within each original coagulating particle of each size move with the total particle to the correct size bin of the resulting aerosol or hydrometeor size distribution. Thus, aerosol particles and their components are tracked within hydrometeor particles through cloud formation and precipitation and to snow or sea ice below. When precipitation falls to snow or sea ice, the aerosol inclusions are added to the top of the snow or ice and slowly migrate through the snow or ice. The inclusions affect radiative heating of the snow or ice layer, as described shortly.

Sea spray and spume drop particles are emitted as a function of size and wind speed into the IM aerosol distribution, accounting for whitecap formation at high wind speed (16, 17). The treatment also accounts for the faster deposition rate of larger spume drops by solving emissions simultaneously with sedimentation. A worldwide sea spray net emission budget from the model is given in (18).

S1.G. Radiative Processes

For radiative calculations, each model column is divided into clear- and cloudy-sky columns, and separate calculations are performed for each. Radiative transfer is solved simultaneously through multiple layers of air and one snow, sea ice, or ocean water layer at the bottom to calculate, rather than prescribe, spectral albedos over these surfaces. Since the model tracks black carbon, brown carbon, soil dust, and all other aerosol inclusions within precipitation, all of which fall onto snow and sea ice, the radiative transfer calculation accounts for the optics of all these absorbing aerosol constituents within and between snow and sea ice particles as well as within aerosol particles and within and between cloud and precipitation particles. The optical properties of snow and sea ice containing absorbing cores are calculated from Mie theory assuming an equivalent radius of snow or ice. The radius varies with the age of the snow as a function of temperature and temperature gradient (19). In sum, the model treats both the microphysical and radiative effects of aerosols on clouds, precipitation, snow, and sea ice.

The radiative code (20) solves for atmospheric heating rates and actinic fluxes over each of 694 wavelengths/probability intervals with gas absorption coefficients from (21). Aerosol and cloud optical properties are calculated by integrating spectral optical properties over each size bin of each aerosol and hydrometeor particle size distribution. In aerosol particles, black carbon is treated as a core surrounded by a mixed shell for Mie optical calculations (22). UV and short-visible absorption by organic carbon is accounted for, allowing for absorption by brown carbon, including tar balls (14, 23, 24). Since all aerosol component concentrations are tracked in each size of each hydrometeor particle type (liquid, ice, and graupel) throughout the evolution of clouds and precipitation, the model accounts for cloud absorption due to soil dust, BC, and brown carbon (BrC) inclusions tracked in size-resolved hydrometeor particles.

For each size of a cloud liquid, ice, or graupel particle; BC, BrC, and soil dust inclusions are treated as polydisperse spherules randomly dispersed throughout cloud particles whose optical properties are calculated with the iterative dynamic effective medium approximation (DEMA) (25, 14).

S1.H. Treatment of Wind Turbine Energy Extraction

In the present study, ~335,400 5-MW onshore wind turbines and ~154,400 5-MW offshore turbines are distributed state-by-state in GATOR-GCMOM according to (4), who estimate the number of turbines needed by state to power nearly 50% of the CONUS all-purpose power supply in 2050. Within each state, wind turbines are placed near where each of 42,000 wind turbines in the U.S. currently exists, as determined by (26, 27).

Many new wind farms are therefore placed within each state in the model. Each wind farm consisted of tens to thousands of turbines. Because of the proximity of wind turbines to each other within a farm, it is necessary to account for competitive extraction of the wind's kinetic energy by all turbines in the model. Failing to account for such interaction results in an overestimate of available wind power.

The numerical treatment of energy extraction by each wind turbine is the same as in (2), but is repeated here for clarity. Due to the coarse horizontal resolution used (4^ox5^o and 2^ox2.5^o globally), wind turbines here are not resolved in the horizontal, but they are resolved in the vertical, with five layers per turbine; nevertheless, all turbines extract the precise amount of energy from the wind as their power curve dictates.

Since, as described below, the power output from a wind turbine is a function of the wind speed at hub height and air density, the extraction of kinetic energy by each turbine in one grid cell reduces the potential power output of other turbines in the same cells and in adjacent grid cells by reducing the wind speed in the same and adjacent grid cells. The reduction in total kinetic energy in a grid cell (and hence the reduction in the wind speed reaching adjacent grid cells) is a function of the number of turbines in each cell and the characteristics of each turbine. We assume that all of the turbines in a cell are the same type and estimate the wind speed at the center of each cell at hub height based on wind speeds at the edge of each cell.

The standard turbine is characterized by a rated power (P_t=5 MW), a rotor diameter (D =126 m), a hub height above the topographical or ocean surface (H=100 m), and a characteristic horizontal spacing area (m^2) $A_{turb}=xD$ x yD, usually determined by convention to minimize interference of the wake of one turbine with the next. In this equation, x and y are constants that provide distances perpendicular to and parallel to, respectively, the prevailing wind direction. The values used for the present study are x=4, y=14.

For determining extraction of kinetic energy, each wind turbine is assumed to intersect several atmospheric vertical layers of a grid column. The momentum extracted from each layer k that the turbine intersects is proportional to the ratio of the swept area of the turbine residing in the layer (S_k) to the total swept area (m^2) of the turbine, $S_{turb}=\pi D^2/4$. The swept area residing in a layer is determined from geometry. For example, the swept area falling in the lowest layer of Figure S1 (ABCDA) is the area HADCH minus the area HABCH. Since the hub height (point H) and the height above the ground of the edge of each layer (e.g., point B) are known, the vertical distance HB is also known. Since the distance HC, which is the turbine radius $R=D/2$, is also known, the angle BHC is $\theta_{BHC}=\arccos(HB/R)$. Therefore, area HADCH=$2\theta_{BHC}S_{turb}/2\pi$, and area HABCH=HB x $R\sin(\theta_{BHC})$. The areas of subsequent layers are calculated from bottom to top in a similar manner, taking into account the summed areas determined already.

Kinetic energy is extracted from each model layer that intersects the turbine rotor each time step Δt due to conversion of the kinetic energy to electric power by the turbine. The model uses the Arakawa C grid structure; thus, u scalar velocities are located at the west (i-1/2,j) and east (i+1/2,j) edges of each grid cell in each layer k, v scalar velocities are located at the

south (i,j-1/2) and north (i,j+1/2) edges, and mass M (kg) and other scalars are located at the center (i,j,k) of the cell. As such, the initial (subscript I) total kinetic energy in grid cell i,j,k before energy extraction is

$$E_{\mathrm{I},i,j,k} = 0.5\left(E_{\mathrm{I},i-1/2,j,k} + E_{\mathrm{I},i+1/2,j,k} + E_{\mathrm{I},i,j-1/2,k} + E_{\mathrm{I},i,j+1/2,k}\right) \tag{S1}$$

In this equation,

$$\begin{aligned}
E_{\mathrm{I},i-1/2,j,k} &= 0.5 M_{i-1/2,j,k} u^2_{\mathrm{I},i-1/2,j,k} \quad where \quad M_{i-1/2,j,k} = 0.5\left(M_{i-1,j,k} + M_{i,j,k}\right) \\
E_{\mathrm{I},i+1/2,j,k} &= 0.5 M_{i+1/2,j,k} u^2_{\mathrm{I},i+1/2,j,k}, \quad where \quad M_{i+1/2,j,k} = 0.5\left(M_{i,j,k} + M_{i+1,j,k}\right) \\
E_{\mathrm{I},i,j-1/2,k} &= 0.5 M_{i,j-1/2,k} v^2_{\mathrm{I},i,j-1/2,k}, \quad where \quad M_{i,j-1/2,k} = 0.5\left(M_{i,j-1,k} + M_{i,j,k}\right) \\
E_{\mathrm{I},i,j+1/2,k} &= 0.5 M_{i,j+1/2,k} v^2_{\mathrm{I},i,j+1/2,k}, \quad where \quad M_{i,j+1/2,k} = 0.5\left(M_{i,j,k} + M_{i,j+1,k}\right)
\end{aligned} \tag{S2}$$

The average horizontal wind speed at the vertical and horizontal center of a cell, used to determine kinetic energy extraction by each wind turbine to produce electricity each time step, is thus $W_{i,j,k}=[2E_{\mathrm{I}i,j,k}/M_{i,j,k}]^{1/2}$. The kinetic energy extracted from all $N_{i,j,k}$ turbines in a given cell during the time step is calculated as

$$\Delta E_{i,j,k} = N_{i,j,k}\, P_{i,j,k}\, \Delta t\, S_k/\mathrm{S}_{turb}, \tag{S3}$$

where $P_{i,j,k}$ is the power extracted from a single turbine at instantaneous wind speed $W_{i,j,k}$ located at grid cell center and based on the turbine's power curve. Equation S3 implies that the power determined from the power curve is calculated with a different wind speed in each model vertical layer intersecting the turbine. Whereas power curves are derived based on the wind speed at hub height, the assumption of varying power extraction for varying heights in the turbine is necessary, since otherwise it would be possible to extract more energy from a layer than is physically present. For example, suppose (in a hypothetical extreme case), the wind speed is 0 m/s in the lowest layer intersecting the turbine and 10 m/s at hub height. Subtracting a portion of the total energy extracted from the lowest layer would be unphysical. Since wind speeds vary roughly logarithmically with height and the height of a turbine swept area is only D, higher wind power extracted at the turbine top are roughly compensated for by lower power extracted at the bottom.

For the REpower 5-MW turbine, a fit to the power curve data, combined with a correction for air density, is

$$P_{i,j,k} = \frac{\rho_a(T,p,q)}{\rho_{a,STP}} \begin{cases} 0 \quad W_{i,j,k} < 3.5002\frac{m}{s} \, or \, W_{i,j,k} > 30\frac{m}{s} \\ 807.69 + W_{i,j,k}\left(-495.51 + W_{i,j,k}\left(77.88 - 0.64W_{i,j,k}\right)\right) \;\; 3.5002 \le W_{i,j,k} \le 10\frac{m}{s} \\ 12{,}800 + W_{i,j,k}\left(-5{,}713.3 + W_{i,j,k}\left(740.0 - 26.667W_{i,j,k}\right)\right) \;\; 10 < W_{i,j,k} \le 13\frac{m}{s} \\ 5000 \qquad W_{i,j,k} > 13\frac{m}{s} \end{cases}$$

based on manufacturer-provided power output versus wind speed, where $\rho_{a,STP}$=1.225 kg/m^3 is air density at standard temperature and pressure and $\rho_a(T,p,q)$ is air density at the current temperature (T), pressure (p), and specific humidity (q). The RE Power turbine power curve indicates a cut-in wind speed of 3.5 m/s, a designed cutout wind speed of 30 m/s, and a rated wind speed of 13 m/s.

The final kinetic energy in each grid cell is $E_{Fi,j,k} = E_{Ii,j,k} - \Delta E_{i,j,k}$. The turbines also convert kinetic energy into turbulent kinetic energy (TKE) since the reduction in wind speed due to the turbine results in wind shear, creating subgrid-scale mechanical turbulence and TKE, which contributes to background turbulence. The TKE is calculated from the level 2.5 TKE closure scheme of (28). The change in total kinetic energy in a grid cell due to power extraction by turbines is next partitioned proportionately among the kinetic energies of the surrounding u and v points, and the final wind speed at each u and v point is then extracted from the kinetic energy as described in the Supplementary Information of (2).

Energy conservation due to power generation and frictional dissipation of winds at the surface is maintained in the model by converting all electric power generated by the wind turbines to heat where the electricity is used. The model also converts kinetic energy lost by natural surface roughness to turbulence and then heat. The electric power generated by turbines each time step, $\Delta E_{i,j,k}$, modifies the surface air temperature (where the electric power is consumed by human activity), as discussed in (2). Kinetic energy or electricity dissipated to heat in the model creates buoyancy, giving rise to potential energy. Gradients in potential energy then regenerate some kinetic energy. Thus, the model conserves energy.

S1.I. Treatment of Solar Energy Extraction by PV Panels and CSP Power Plants

The model is further modified here to treat extraction of energy from residential rooftop photovoltaic (PV) systems, commercial/government rooftop PV systems, utility-scale PV systems, and concentrated solar power (CSP) systems (Table S2). In GATOR-GCMOM, utility-scale PV and CSP plants are placed in desert or low latitude regions in each state, and rooftop PV is placed in urban areas according to the state distributions of these generators given in (4).

The model predicts time-dependent direct and diffuse solar radiation as a function of wavelength and altitude, accounting for time-dependent predicted gas, aerosol particle, and cloud concentrations and optical properties in the atmosphere. The radiative transfer calculations (Section S1.G) also accounts for surface albedo and temperature, building and vegetation shading, angle of the sun, Earth-sun distance, Earth-space refraction, and solar intensity versus wavelength. As such, the model predicts the variable nature of solar radiation fields.

Each solar PV panel for rooftop and utility solar in the model is assumed to be a SunPower E20 435 W panel with panel area of 2.1621 m^2, giving a panel efficiency (watts of power output per watt of solar radiation incident on the panel) of 20.1%. The cell efficiency (power out per watt incident on each cell) is 22.5%. Each CSP plant before storage is assumed to

have the characteristics of the Ivanpah solar plant, which has 646,457 m^2 of mirrors and 2.17 km^2 of land per 100 MW installed power and a CSP efficiency (fraction of incident solar radiation that is converted to electricity of 15.796%, calculated as the product of the reflection efficiency of 55% and the steam plant efficiency of 28.72% (29).

Solar PV and CSP in the model extract power, reducing temperatures of the surfaces of rooftops or ground over which the PV and CSP lie. However, because electricity use results in the dissipation of electrical energy to heat, the heat from the electricity use is subsequently released to the air. As such, the model conserves energy extracted by PV and CSP as it does with wind turbines. However, in the case of solar, the extracted energy does not affect either the available solar energy or the performance of the solar-power system.

S1.J. Maturity of WWS and Storage Technologies and Uncertainties of Some Assumptions

Most of the WWS electric power producing technologies considered, including onshore and offshore wind turbines, solar photovoltaics, CSP plants, geothermal plants, and hydropower plants, are mature technologies. For example, as of the end of 2014, 363 GW of onshore wind, 8.8 GW of offshore wind, 173 GW of solar PV (rooftop plus utility scale), 5.7 GW of CSP, 12.6 GW of geothermal for electricity, and 1,143 GW of hydropower had been installed worldwide, On the other hand, only 0.53 GW of tidal plus wave power had been installed, with almost all of this being tidal. Nevertheless, only ~0.5% of total installed power under the U.S. plans is proposed to be tidal plus wave, so even if these technologies do not ramp up significantly, they can be replaced by other WWS technologies.

With respect to electric power storage technologies, pumped hydropower storage (PHS), hydropower, and CSP with molten salt storage are mature technologies. Whereas, PHS is commonly used primarily for short-terms storage (hours to days between charging and discharging), hydropower discharging can be used to supply short- or long-term gaps in power. In this study, hydropower discharging is used as a last resort to fill gaps in supply. The use of phase-change materials with CSP is less mature than is the use of molten salt with CSP, but its lower cost is expected to drive up its use in comparison. Storage of heat in water and cold in water and ice are mature technologies. Storage of heat in soil has been tested successfully under extreme conditions in Drake Landing and other communities (e.g., 30).

One set of key assumptions in this study is that certain percentages of different loads can be met with thermal energy storage, hydrogen, or DR (Table 1, Column 4). For example, we assume 85-95% of air and water heating and air-cooling loads can be met with storage or DR. However, there is no technical or economic reason why 100% of such loads cannot be met with previously stored heat and cold in water, ice, and/or soil with the WWS system proposed here. Thus, we think the assumption that less than 100% of such loads are tied to storage is conservative.

Similarly, we assume that 85% of transportation loads can be met with DR or hydrogen. Vehicles are parked most of the day and night, either at workplaces or residences, enabling utilities to enter into contracts with users to supply electricity sometime during the period of parking, not necessarily continuously. Similarly, hydrogen, which will be used primarily for

long-distance trucking, heavy ships, and aircraft, can be produced by WWS electricity during any time of a year.

S1.K. Simulations and Comparisons With Data

Previous paired-in-time-and-space GATOR-GCMOM model predictions of wind and solar resources have been compared with data in (3, 13, 31). Modeled wind fields with satellite or other model data have been compared in (2, 3 Supplemental Information).

The GATOR-GCMOM model is run here for six years (2050-2055) assuming the U.S. is converted to 100% WWS. The base-case model resolution is 4ºx5º in the horizontal. A separate, 2-year simulation is run at a horizontal resolution of 2ºx2.5º. In both cases, the model includes 68 sigma-pressure layers from the ground to 0.219 hPa (≈60 km), with 15 layers in the bottom 1 km and 500-m resolution from 1-21 km. The dynamical time step (for predicting winds) is 30 s.

In a baseline case, the LOADMATCH grid integration model is run for six years with a 30-s time step using wind and solar inputs from a GATOR-GCMOM simulation and load data extrapolated to 2050-2055 as described in the main text. To test the robustness of the model, LOADMATCH is also run separately and successfully for each of the six years using either the 2050 or 2051 load data (thus 12 more simulations) and by reversing the 2050-2055 load time series but using the 2050-2055 WWS supply time series without reversing it (1 simulation). Thus, an ensemble of 14 LOADMATCH simulations, including the baseline simulation, is performed with 4ºx5º WWS data. The computer time required for LOADMATCH to solve each six-year simulation on a single Intel Nehalem 5580 3.2 GHz processor is 3-4 minutes.

LOADMATCH is run further for two years using the 2ºx2.5º GATOR-GCMOM simulation wind and solar data with 2050 and 2051 load data in that order and with 2051 and 2050 load data in that order (2 more simulations). It is then run separately using 2050 WWS data and 2050 load data; 2050 WWS data and 2051 load data; 2051 WWS data and 2050 load data; and 2051 WWS data and 2051 load data (4 more simulations). Thus, an ensemble of six simulations is performed with 2ºx2.5º WWS data.

Further, many sensitivity simulations relative to the baseline simulation are run by varying a single parameter at a time in LOADMATCH (Table S3).

Figure 1 of the main text shows the impacts of kinetic energy extraction by wind turbines from the baseline six-year GATOR-GCMOM simulation versus a simulation with no kinetic energy extraction.

Figure S2 here shows the raw 2006 and 2007 time-dependent U.S. loads, and Figure S3 shows the same, but focused on a 20-day period of peak load.

Figure 2 of the main text shows LOADMATCH baseline-simulation results monthly for the full six-year period. Figures 3-4 of the main text show two four-day periods (one in summer and the other in winter, respectively) during the six-year baseline simulation at higher

resolution. Figures S4-S6 show additional hourly results for different four-day periods during the baseline simulation.

Figures S7-S19 show the sensitivity, over six years of LOADMATCH simulation, of the average costs of energy to different assumptions and parameters. The sensitivity results, summarized in Table S3, indicate the scheme is robust and solves with zero loss of load under a variety of conditions. Of particular interest is the result in Figure S14, which indicates that the system is stable even without DR by instead increasing electricity demand while reducing the need for storage. This exchange is performed with no large difference in cost.

Remaining LOADMATCH results using the 4ºx5º GATOR-GCMOM simulation wind and solar time-dependent output but with different combinations of load and WWS resources, and results using the 2-year 2ºx2.5º GATOR-GCMOM simulation output indicate zero loss of load as well at virtually the same cost as in the baseline case.

S1.L. Standard for Reliability

The electric utility industry standard for reliability is a loss of load expectation (LOLE) of 1 day (24 hours) in 10 years. Loss of load can arise due to scheduled or unscheduled maintenance of energy generators, random variation in load or WWS resources, and transmission congestion.

LOADMATCH treats these losses as follows. First, losses of energy due to down time from scheduled and unscheduled maintenance, typically 0-1% for solar power plants and 2% for wind plants (32), are included as an energy loss together with transmission and distribution losses. However, assuming that the energy loss from a single down wind turbine equals the loss of energy available to consumers overestimates energy loss to consumers. The reason is that, when a single wind turbine is down, all the other turbines in a wind farm receive and extract more kinetic energy because of lesser competition among turbines for the limited kinetic energy available (Figure 1), so the aggregate power loss among all turbines is slightly less than the power lost to the down turbine. The impact of this is that our assumption that energy loss is proportional to down time is conservative in that it slightly overestimates energy loss to consumers.

Uncertainties in load and WWS resources are accounted for in the extremely variable nature of the load data (Figures S2, S3) and modeled wind and solar resources used in this study, respectively, as well as in the successful use of an ensemble of 20 load and WWS data sets under the same initial conditions and parameter values (Section S1.K).

Although the impact of transmission congestion on reliability is not modeled explicitly, sensitivity tests are run to check the impact on cost of different fractions of wind and solar power produced subject to long-distance transmission (Figure S13). The implication of Figure S13 is that, if congestion is an issue at the baseline level of long-distance transmission, increasing the transmission capacity will relieve congestion with only a modest increase in cost. Even with all wind and solar subject to long-distance transmission,

the mean cost of the overall system is still only ~12.1 ¢/kWh (versus 11.37 ¢/kWh in the baseline simulation).

Also, although not modeled, grid frequency regulation is provided by ramping up/down hydropower, stored CSP or PHS; ramping down other WWS resources and storing the electricity in heat, cold, or hydrogen rather than shedding; and using demand response.

Future work could include treating the U.S. transmission and distribution grid explicitly although that would likely increase computing time by 4-5 orders of magnitude given the need to iterate over thousands of buses in a power load flow model to obtain an equilibrium solution. The current model requires no iteration but simplistically assumes a fully interconnected grid, but it does account for line loss. The use of a load-flow model may not provide much more accuracy because of the uncertainty of exactly where all WWS generators will be placed in each state and what size each line will be in each location.

One minor inconsistency among data sets used here is that the wind and solar data are derived from GATOR-GCMOM runs for the years 2050-2055, but the load data are based on monthly average heating and cooling degree-days from 1949 to 2011 and hourly load patterns from 2006 and 2007. However, because both load and WWS supply data are aggregated over CONUS for this study, they are roughly consistent with each other on both the diurnal and seasonal scales. For example, high heat loads occur during winter due to low temperatures. The climate model also predicts low temperatures during winter, and the resulting winds and solar fields are consistent with the low temperatures and other meteorological conditions causing them. Thus, the same physical processes affecting winds and solar in the climate model affect loads on seasonal and diurnal scales. Finally, the sensitivity runs considered here cover even relatively diverse combinations of supply and demand.

S1.M. Stochastic Versus Deterministic Nature of Simulations

A deterministic model is one in which the model output is fully determined by the parameter values, initial conditions, and time-dependent inputs. In other words, the model always produces the same output from a given initial state, thus the model output is effectively pre-determined (33).

A stochastic model is one whose final state is determined randomly by varying one or more time-dependent inputs randomly. Multiple runs of a stochastic model, where time-dependent inputs are varied randomly using a probability distribution, lead to a probability distribution of the output (34). Whereas, each simulation in a stochastic model is deterministic since there is only one possible output for each time series of randomly generated inputs, the collection of multiple deterministic outputs results in a stochastic probability distribution of output, thus a stochastic model.

In the LOADMATCH grid integration model, the baseline parameter values and initial conditions are pre-set, but different time-series of input loads and WWS supplies are used. Time-varying wind and solar resources are predicted over time with a 3-D climate model

that accounts for physical meteorology and chaotic variation. Different time series can be generated by, for example, changing the horizontal resolution of the 3-D model.

LOADMATCH simulations here are similar to those of a pure stochastic model in that each simulation with LOADMATCH is run with the same initial conditions and parameter values but with an ensemble of 20 different time series of loads and WWS supplies (Section S1.K) to obtain an ensemble of stable results. In a pure stochastic model, each time series of loads and WWS supply would be randomly generated to obtain a probability distribution of results rather than just an ensemble of results.

LOADMATCH places the highest priority for system planning on reliability by ensuring that the load is met each time step. The focus on reliability reflects how actual systems are organized, namely based on planning reserve margins or probability-based metrics [e.g., loss of load expectation (LOLE), loss of load probability (LOLP), energy use efficiency (EUE)]. Other aspects of planning and operating the grid, such as system cost and stability (e.g., frequency control, transient stability) are also important for practical operation of the grid and should be considered in future work. Resiliency and security are lower priority elements but are nevertheless topics of interest as well.

Because of its flexibility, LOADMATCH can readily be modified to meet a standard of reliability less than 100%. This will result in even lower-cost but less reliable WWS energy and storage mixes than those found here. The model can also be modified to treat different WWS generators, loads, and storage capacities and can be applied to any region of the world given sufficient inputs.

While converting LOADMATCH from a trial-and-error model to a least-cost or least-carbon optimization model may be possible, the disadvantages of such a conversion are (1) stable solutions may not be obtainable over the numerous variables treated here and (2) solutions obtained may require at least 4-5 orders of magnitude more computer time for just one simulation than the 3-4 minutes required here. Many optimization codes today solve for only a limited number of variables because of these two constraints. For the present study, the goal is not necessarily to find the lowest cost of a system, only to show that some low-cost solutions exist. The present tool performs this task.

Finally, while this study attempts to provide a theoretical framework for determining the storage and DR needed to allow projected state-by-state WWS supply to match CONUS load, practical implementation of the solution requires real investment and infrastructure improvements. The details of the spatial distribution of the T&D infrastructure upgrades, such as the extent of the use of microgrids and the integration of CONUS with Canadian and Mexican power systems, and the exact locations within each state of WWS generators, are not provided herein.

However, the results of this study can inform planners and policy makers about what the main ingredients of a fully integrated system should include – namely the approximate numbers and sizes of WWS generators and storage devices and some characteristics of the T&D system. As such, this study and further studies using this model in other regions may

reduce barriers toward the implementation of fully integrated clean, renewable, and reliable energy systems worldwide.

S2. Supporting Tables

Table S1. Lifecycle costs, round-trip efficiency, nameplate charge/discharge capacity of each storage technology assumed in this study.

Storage technology	Capital cost of storage beyond power generation ($/maximum-deliverable-kWh-th)	Round-trip charge/store/ discharge efficiency (%)	Assumed maximum charge (discharge) rate of technology (GW)	Assumed energy storage capacity (maximum-deliverable TWh)	Percent of total storage in this technology (%)
Non-UTES					
PHS	[1]14.0 (12-16)	[6]80	[10]57.68 (57.68)	0.808	5.42
STES	[2]6.5 (0.13-12.9)	[2,7]70	[11]42.11 (42.11)	0.590	3.95
PCM-ice	[2,3]36.7 (12.9-64.5)	[2]82.5	[12]18.05 (18.05)	0.253	1.69
PCM-CSP	[4]15.3 (10-20.0)	[8]99	[13]947.2 (362.9)	13.26	88.94
Total or average	**15.2 (9.77-20.3)**	**96.5**	**1,065 (480.8)**	**14.91**	**100**
UTES	**[5]0.90 (0.071-1.71)**	**[9]56**	**[14]466.9 (714.7) 1,072.0**	**514.6**	**100**

UTES = Underground thermal energy storage. PHS = pumped hydropower storage; STES = Sensible heat thermal energy storage; PCM = Phase-change materials; CSP=concentrated solar power; All storage is for 14 hours except UTES (see last footnote).

[1](35).

[2](36).

[3](37).

[4](38) provide the cost of the phase-change material and storage tanks. The cost of CSP mirrors and other components needed to heat the phase-change material that is put in storage is accounted for in the capital cost of CSP (Table S2).

[5](39), (30).

[6](40). PHS efficiency is the ratio of electricity delivered to the sum of electricity delivered and electricity used to pump the water.

[7](41). STES efficiency is the ratio of the energy returned as cooling after storage to the energy in the electricity input into storage.

[8](42). The PCM-CSP efficiency is the ratio of the heat available for the steam turbine after storage to the heat from the solar collector that goes into storage. The energy losses due to reflection and absorption by the CSP mirrors (45% of incident solar energy) and due to converting CSP heat to electricity (71.3%) (33) are accounted for in the CSP efficiency without storage.

[9](43) The UTES efficiency is the fraction of heated fluid entering underground storage that is ultimately returned during the year (either short or long term) as air or water heat for a building.

[10]PHS storage charge/discharge rate equals U.S. installed PHS capacity plus pending licenses and preliminary and pending preliminary permits (44).

[11]STES storage charge/discharge rate is set equal to 70% of the air conditioning plus refrigeration flexible load from Table 1.

[12]PCM-ice storage charge/discharge rate is set equal to 30% of the air conditioning plus refrigeration flexible load from Table 1.

[13]The PCM-CSP storage charge rate is ~2.61 times the discharge rate, which is the rated power of the steam turbines in the plants (Table S2).

[14]The maximum charge rate of heat (0.4669 TW) to UTES storage is limited by the installed capacity of the solar thermal collectors (Table S2). The maximum charge rate of stored UTES heat from excess electricity is 1.072 TW. The UTES storage capacity is 514.6 TWh, which satisfies 20 days of charging at the maximum

charge rate from electricity and 30 days of discharging at the peak winter air plus water heat load (0.7147 TW).

Table S2. CONUS installed WWS electric/thermal generator installed capacities in 2013 and proposed for 2050, along with capital costs of the generators and numbers of devices.[1]

	CONUS installed 2013 (GW)	Proposed existing plus new CONUS 2050 installed (GW)	Capital cost new installations ($ million/MW)	Rated capacity per device (MW)	Total number existing plus new CONUS devices 2050
Onshore wind	60.8	1,677	1.49 (1.28-1.70)	5	335,422
Offshore wind	0	771.9	3.77 (2.69-4.85)	5	154,387
Residential PV	3.46	376.8	3.22 (2.71-3.73)	0.005	75.36 mil.
Commercial/government PV	1.73	274.9	2.44 (2.21-2.68)	0.1	2.750 mil
Utility-scale PV	1.73	2,316	1.70 (1.56-1.85)	50	46,329
CSP with some storage[2]	0	362.9	5.19 (4.45-5.92)	100	3,629
Geothermal[3]	2.38	20.74	4.19 (2.49-5.89)	100	207
Hydropower[4]	87.42	87.48	2.82 (2.40-3.25)	1300	67.3
Wave[3]	0	26.20	6.81 (6.08-7.54)	0.75	34,926
Tidal[3]	0	8.25	4.30 (3.72-4.89)	1	8,082
Solar thermal for UTES[5]	0	466.9	1.32 (1.27-1.38)	50	9,380
Total or average	**157.5**	**6,390**	**2.23 (1.90-2.57)**		

[1]Data are from (4) and references therein. except solar thermal collectors are added (footnote 5) and the installed capacity of CSP is increased here (footnote 2).

[2]The CSP generator capacity is increased here by 70% over that needed to fulfill CSPs partial role in providing 100% of all CONUS energy before considering storage charge/discharge rates or losses (4). It is found here that increasing the discharge rate of CSP storage is advantageous for providing peaking power when current electricity load exceeds supply. In the present case, this requires adding additional steam turbines over the base number in (4). Here, it is also found that the ideal ratio of CSP storage capacity to generator capacity is 2.61, which is lower than the assumed ratio in a CSP plant with full storage, 3.2 (4). The capital cost of CSP with no storage is $3.66 (3.29-4.03) million/MW and that with storage 3.2 times the installed generator capacity is $5.75 (4.88-6.62) million/MW (including the cost of extra mirrors and land but excluding costs of phase-change material and storage tanks, which are given separately in Table S1) (4). For the base case here, the ratio of storage to generator capacity is 2.61 rather than 3.2. Interpolating between the no storage and storage costs gives an approximate cost of CSP with storage at 2.61 times generator capacity here of $5.19 (4.45-5.92) million/MW.

[3]Geothermal and tidal provide base-load power that is distributed evenly each model time step. Wave power, which represented < 0.4% of delivered power, is distributed with the same variability as model-predicted winds each time step. Solar thermal is similarly distributed each time step with the same temporal variation as solar PV.

[4]Hydropower use varies during the year but is limited by its annual power supply. When hydropower storage increases beyond a limit due to non-use, hydropower is then used for peaking before other storage is used.

[5]The 2012 bulk cost of solar thermal collector with aperture area of 4'x10' (3.716 m^2) ranges from $3600-$4000 (45). With an installed capacity to aperture area ratio of 0.7 kW-th/m^2 (46) and accounting for technology improvements gives an estimated 2050 cost (in 2013 dollars) from (4) of $1.32 (1.27-1.38) million/MW-th. UTES costs for storage are separate costs provided in Table S1. All solar thermal heat collected is assumed to be transferrable to UTES or used immediately.

Table S3. Sensitivity of mean levelized cost of energy (LCOE) from Table 2 of the main text to various parameters over the listed value range.

Figure	Parameter description	Sensitivity range (baseline value)	[1]Total LCOE (¢/kWh)	Description in text
S7	Max hours of H_2 storage[2]	2304-2880 (2400)	11.37-11.37	Section 2.3
S8	Max charge rate (TW) UTES from solar thermal	459-516 (466.9)	11.37-11.41	Table S2
S9	Max charge rate (TW) non-UTES storage	1.059-1.100 (1.065)	11.37-11.41	Table S1
S10	Max hours of non-UTES storage	8-30 (14)	11.33-11.50	Table S1
S11	Max hours UTES storage at max solar charge rate[3]	389-550 (480)	11.33-11.41	Table S1
S12	Max UTES storage capacity (TWh)	473-686 (514.6)	11.36-11.45	Table S1
S13	Percent of wind & solar subject to LD transmission	0-100 (30)	11.05-12.13	Table 2, fn j
S14	Max hours load can be shifted forward by DR	0-12 (8)	11.37-11.38	Section 2.1
S15	PCM-ice storage efficiency (%)	45-90 (82.5)	11.37-11.37	Table S1
S16	PHS storage efficiency (%)	69-90 (80)	11.37-11.37	Table S1
S17	UTES storage efficiency (%)	55-70 (56)	11.37-11.37	Table S1
S18	PCM-CSP storage efficiency (%)	98-100 (99)	11.37-11.37	Table S1
S19	Transportation load flexibility (%)	80-100 (85)	11.37-11.37	Table 1

UTES = Underground thermal energy storage. PHS = pumped hydropower storage; PCM = Phase-change materials; CSP=concentrated solar power; DR = Demand response; LD = long-distance; fn = footnote.

[1]The baseline mean LCOE is 11.37 ¢/kWh (Table 2). The listed cost ranges are the mean LCOEs resulting from varying each given parameter by the given range.

[2]The baseline maximum H_2 stored energy of 432 TWh is obtained by multiplying 0.18019 TW of H_2 load (Table 1) by 2,400 hours of storage.

[3]The baseline 480 hours of UTES storage satisfies the 514.6 TWh capacity at a charge rate of 1.072 TW (Table S1).

S3. Supporting Figures

Figure S1. Illustration of how the swept area of a single wind turbine intersects multiple model vertical layers in a single grid column. Points A, B, C, D, and H are discussed in the text. From (2).

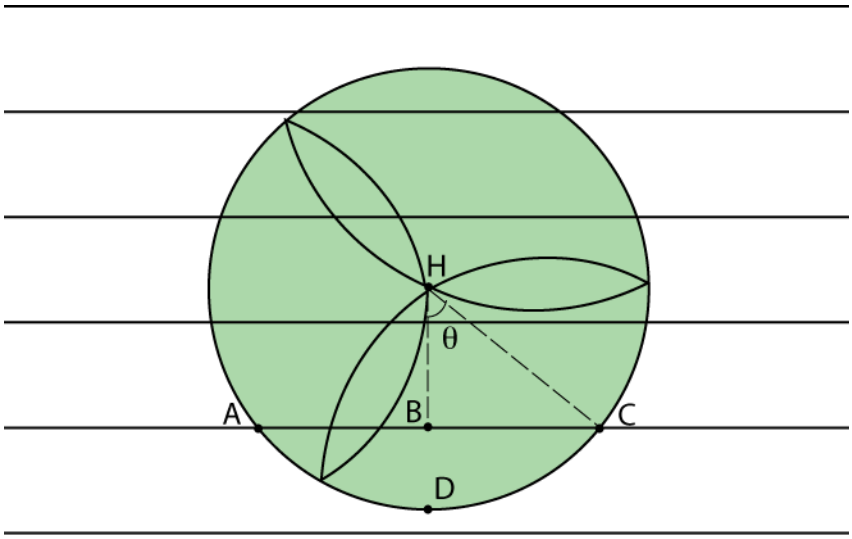

Figure S2. Time-dependent (GMT time) U.S. end-use loads in 2006 and 2007 (47, 48). The average load in 2006 is 437.51 GW and that in 2007 is 450.14 GW.

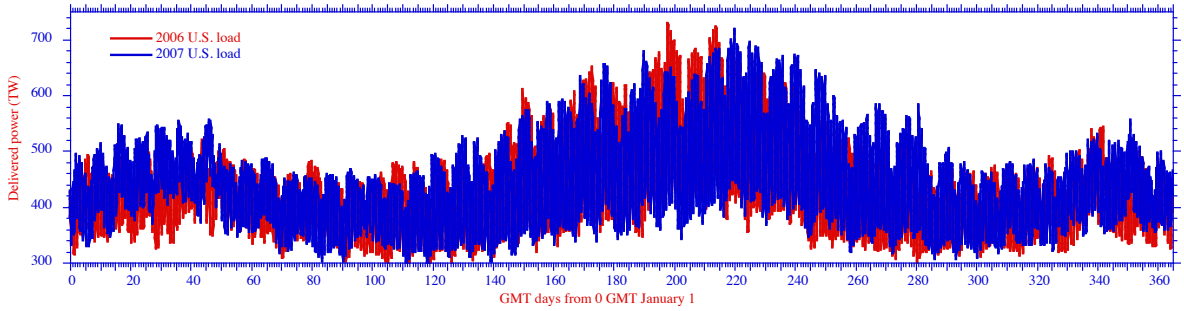

Figure S3. Same as Figure S2, but for a peak 20-day period (47, 48).

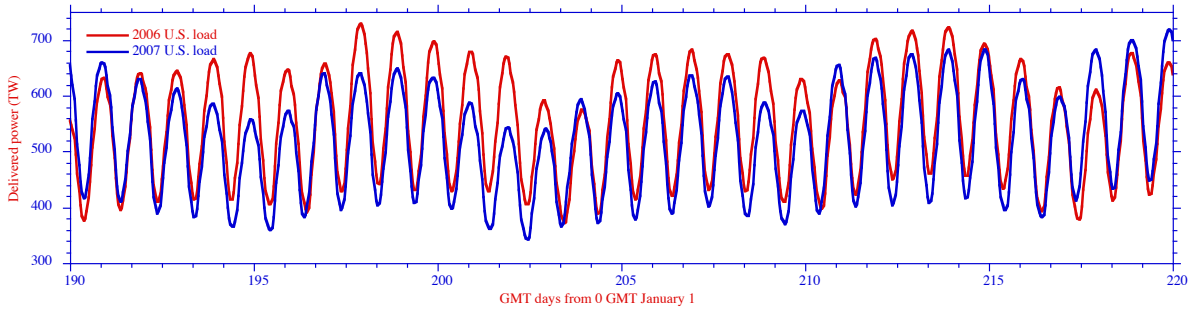

Figure S4. Same as Figure 3, but with hourly results for November 8-11, 2050.

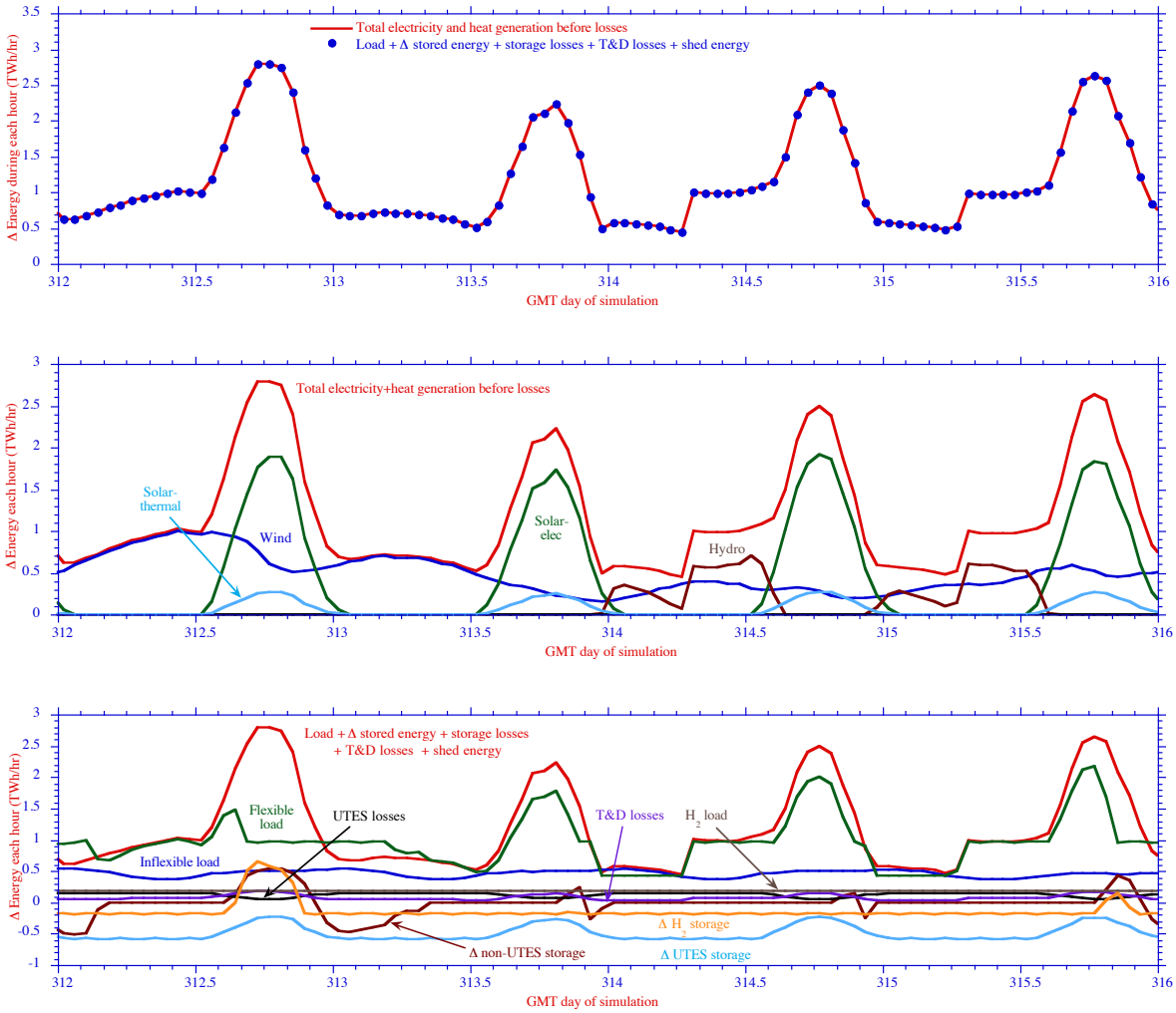

Figure S5. Same as Figure 3, but with hourly results for September 4-7, 2051.

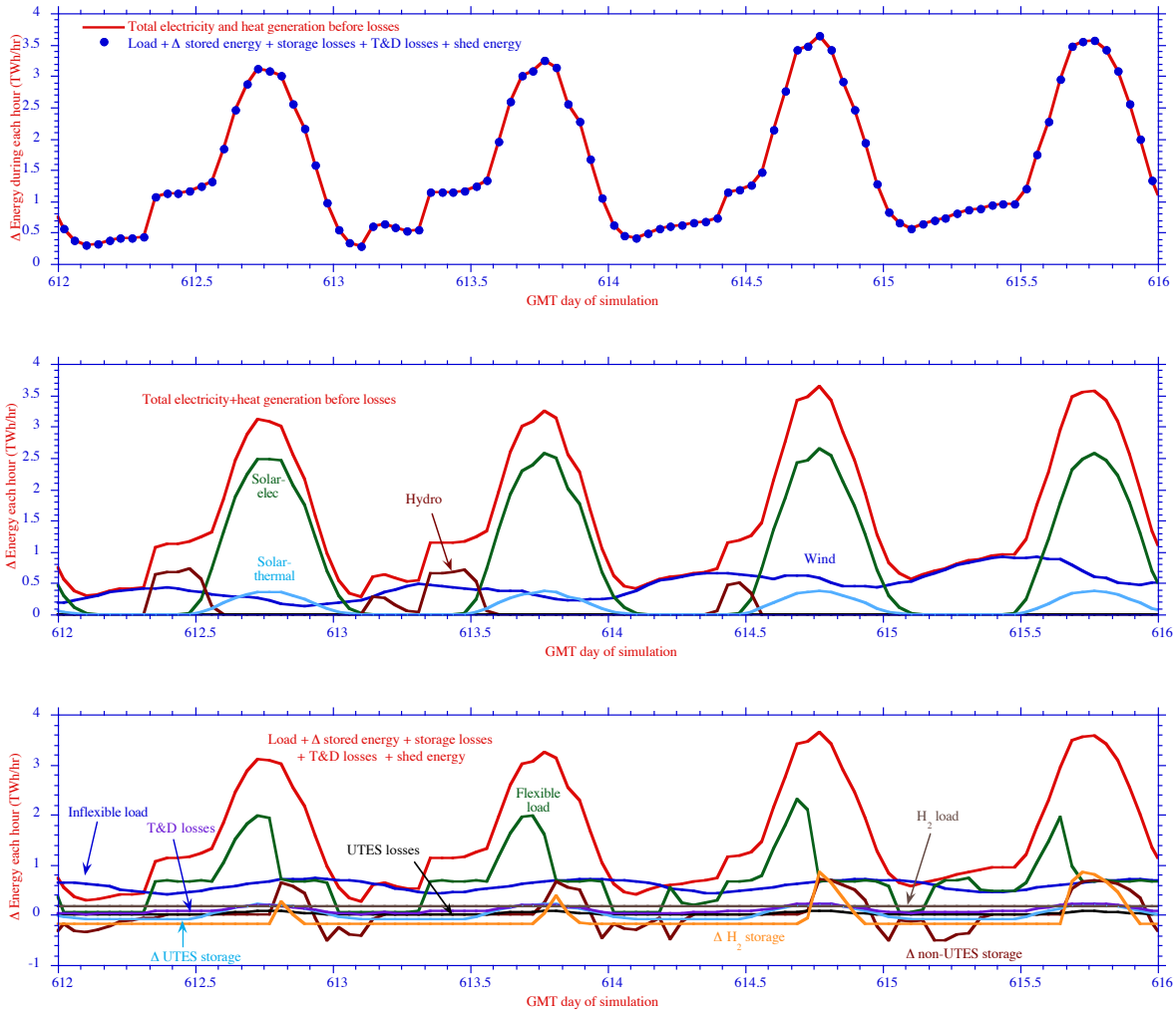

Figure S6. Same as Figure 3, but with hourly results for January 31-February 3, 2053.

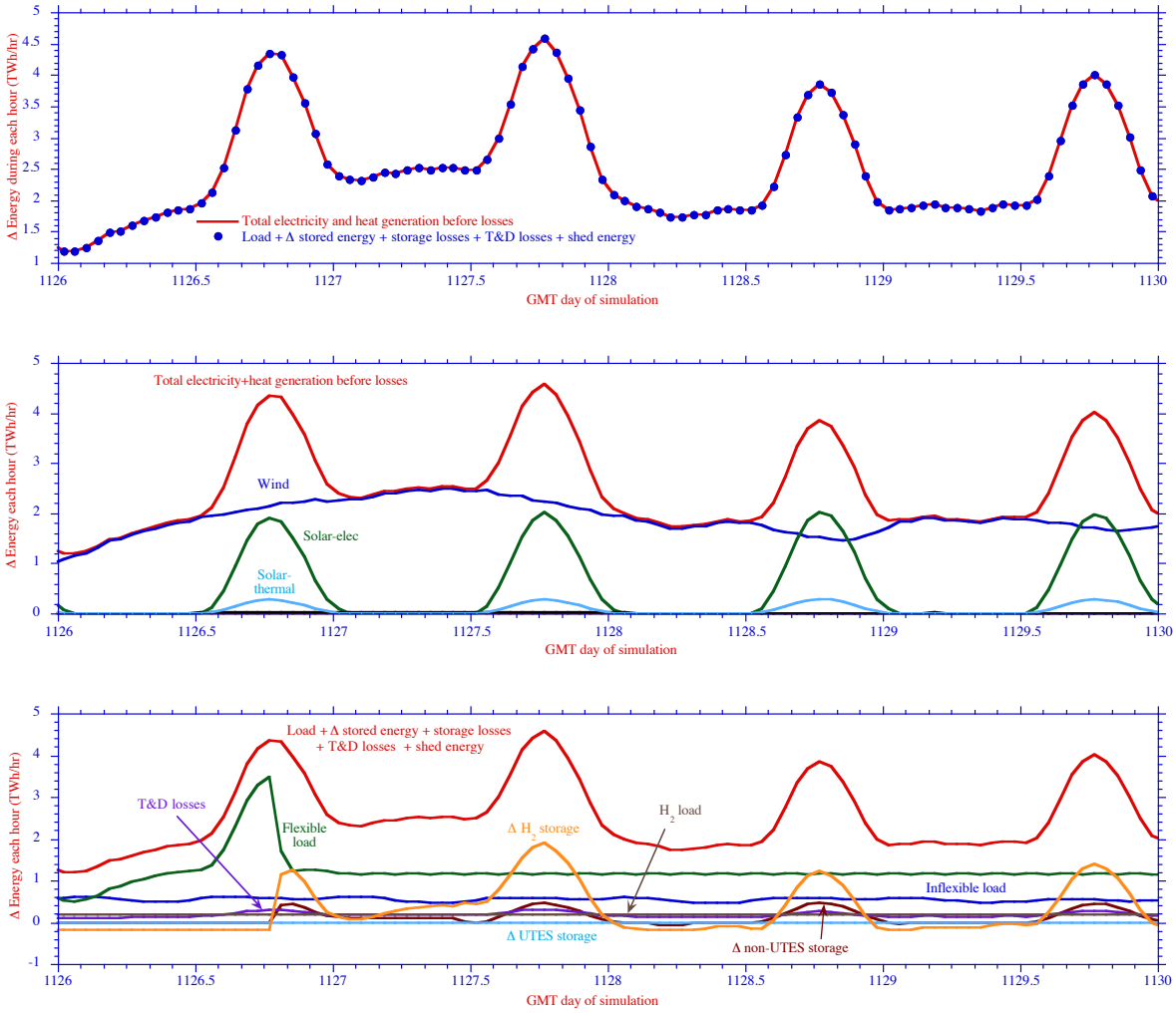

Figure S7. Sensitivity of the mean value and uncertainty range in the levelized cost of energy (LCOE) to the maximum number of hours of hydrogen storage permitted. All other parameters are as in the baseline case. The baseline number of hours of hydrogen storage is 2,400 and cost is 11.37 (8.5-15.4) ¢/kWh (Table 2). Baseline values are bolded. Magenta, cyan, red, green and blue error bars show cost uncertainties from electricity/heat/local transmission, H_2 production/compression/storage, UTES Storage, Non-UTES storage, and long-distance transmission costs, respectively.

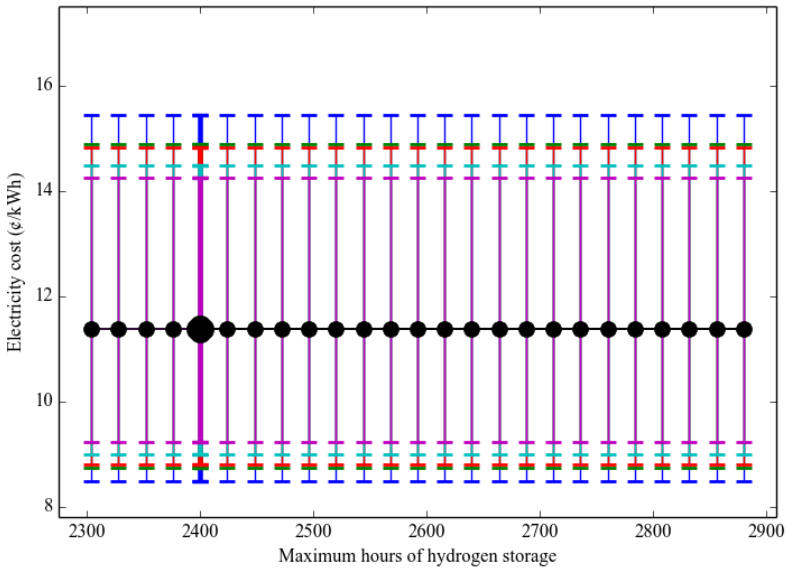

Figure S8. Same as Figure S7, but for sensitivity of the LCOE to 2050 charge rate (GW) of UTES storage from solar thermal collectors (= maximum installed capacity of UTES collectors). Baseline value = 466.9 GW.

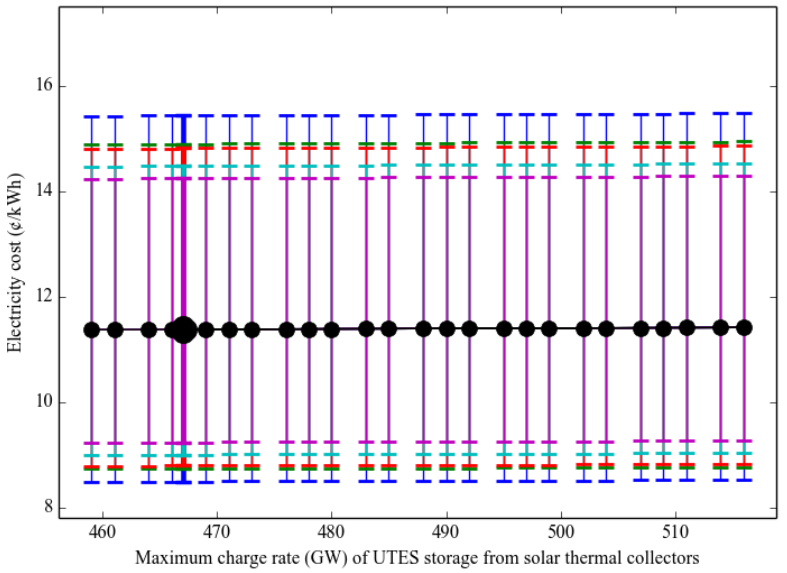

Figure S9. Same as Figure S7, but for sensitivity of the LCOE to the assumed maximum charge rate (TW) of non-UTES storage technologies. Baseline value = 1.065 TW.

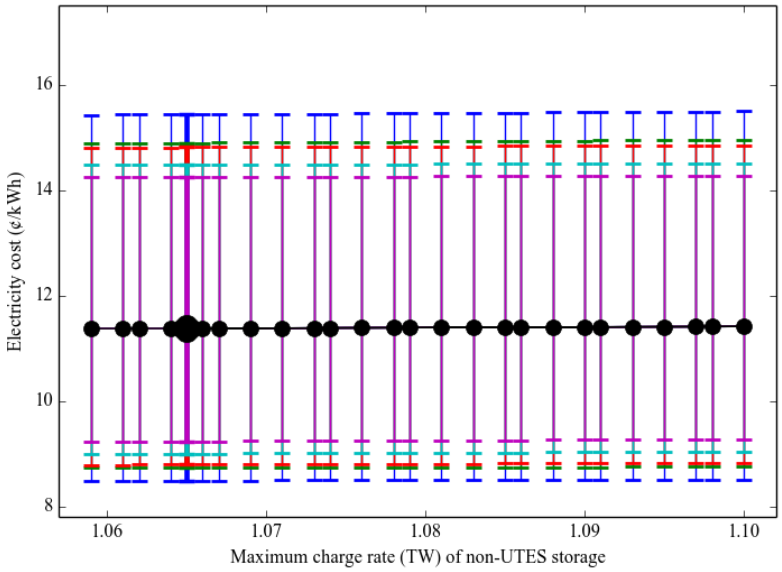

Figure S10. Same as Figure S7, but for sensitivity of the LCOE to the maximum hours of non-UTES storage. Baseline value = 14 hours.

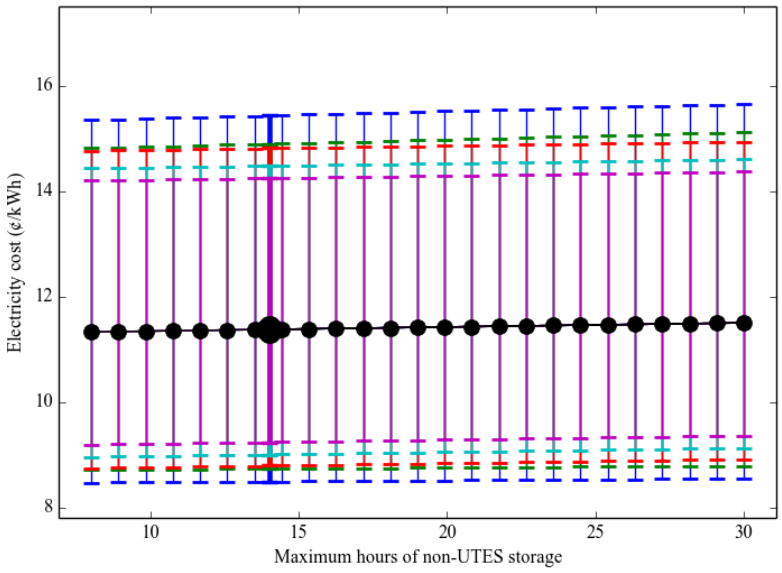

Figure S11. Same as Figure S7, but for sensitivity of the LCOE to the maximum hours of UTES storage. Baseline value = 480 hours.

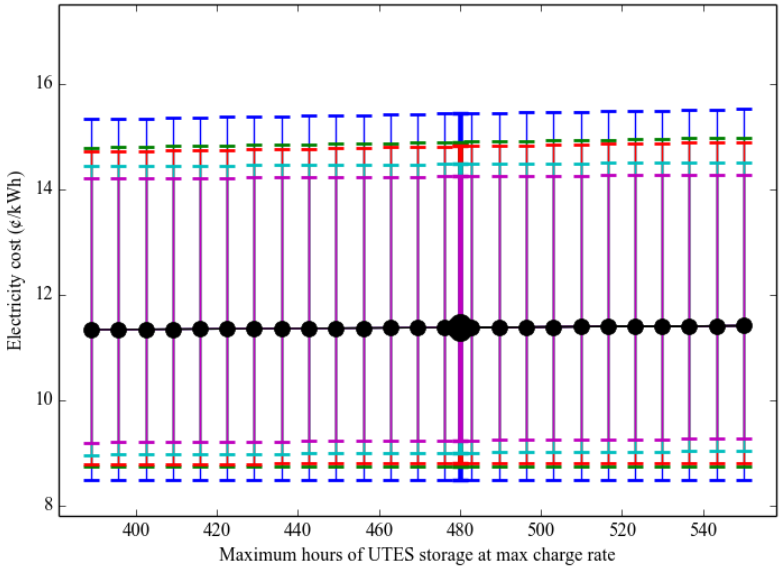

Figure S12. Same as Figure S7, but for sensitivity of the LCOE to the assumed maximum capacity (TWh) of UTES storage. Baseline value = 514.6 TWh.

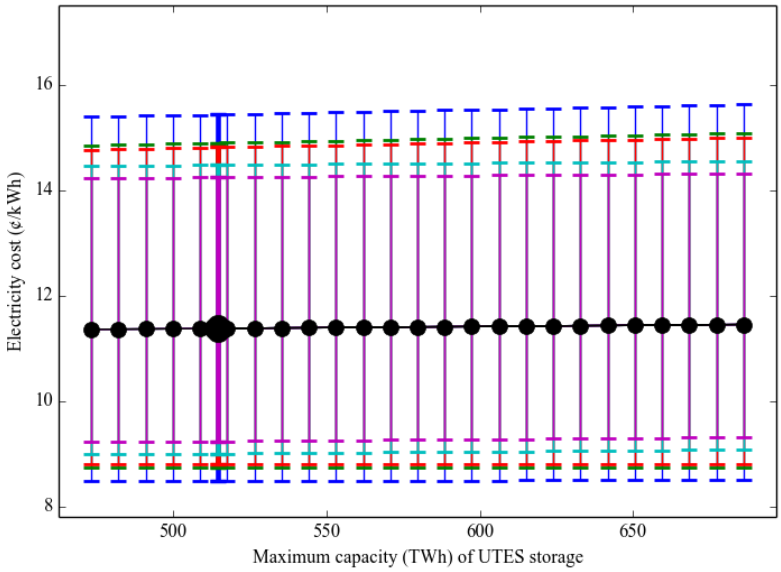

Figure S13. Same as Figure S7, but for sensitivity of the LCOE to the percentage of all generated wind and solar electric power that is subject to long-distance transmission. Baseline value = 30%.

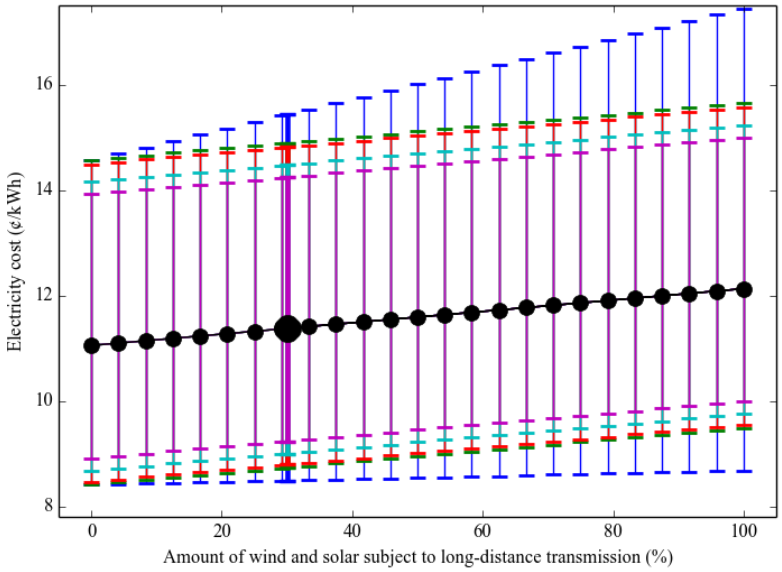

Figure S14. Same as Figure S7, but for sensitivity of the LCOE to the maximum number of hours load can be shifted by DR management before becoming inflexible. Baseline value = 8 hours.

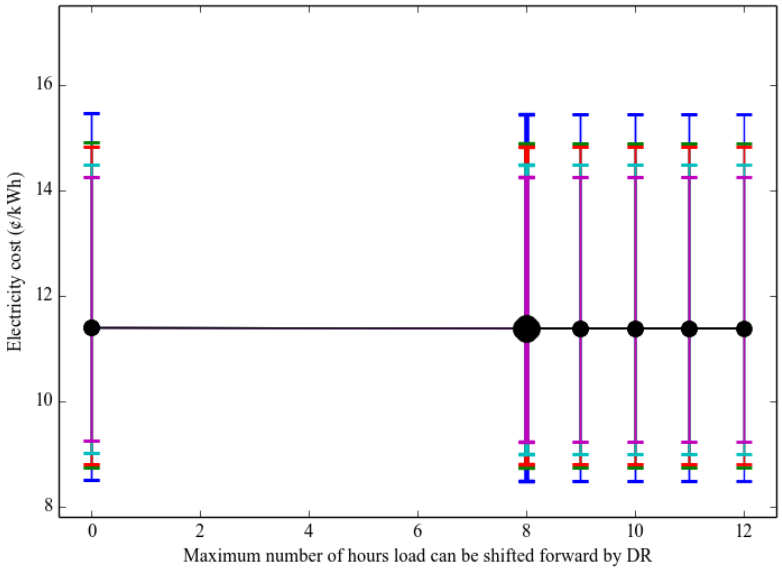

Figure S15. Same as Figure S7, but for sensitivity of the LCOE to round-trip efficiency of storage coupled with ice production and melting (PCM-ice). Baseline value = 82.5%.

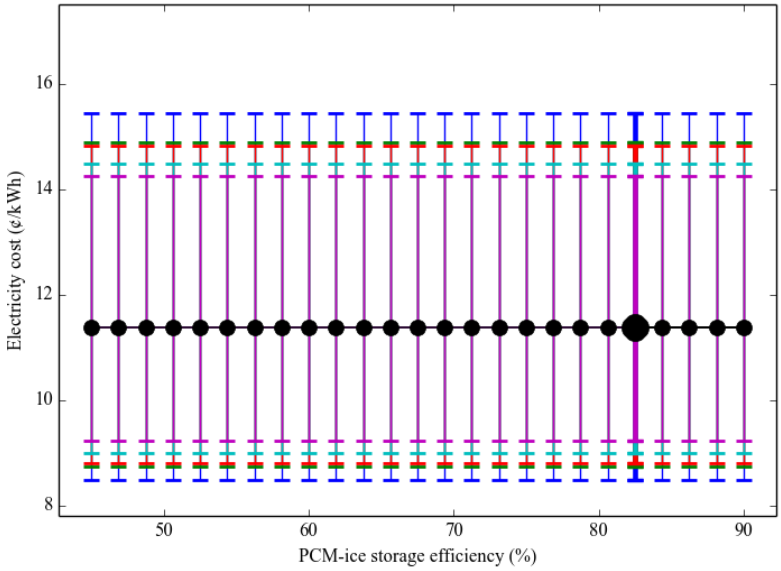

Figure S16. Same as Figure S7, but for sensitivity of the LCOE to round-trip efficiency of pumped hydropower storage (PHS). Baseline value = 80%.

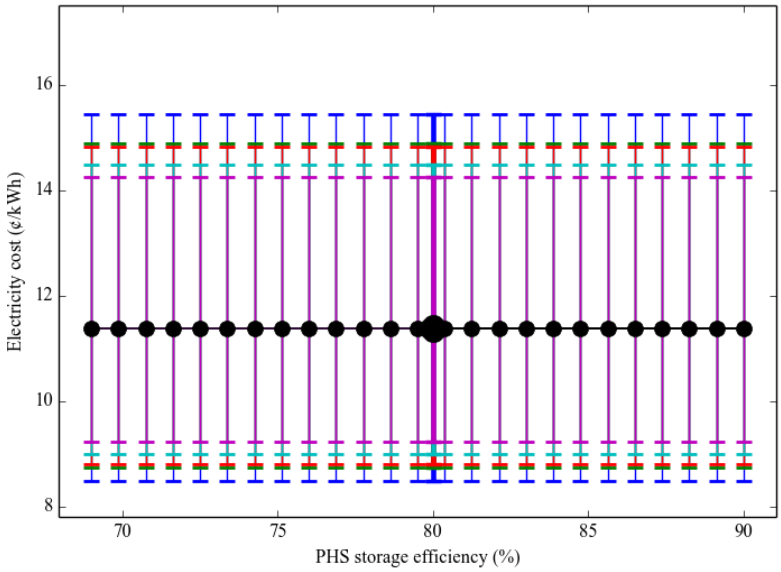

Figure S17. Same as Figure S7, but for sensitivity of the LCOE to round-trip efficiency of underground thermal energy storage (UTES). Baseline value = 56%.

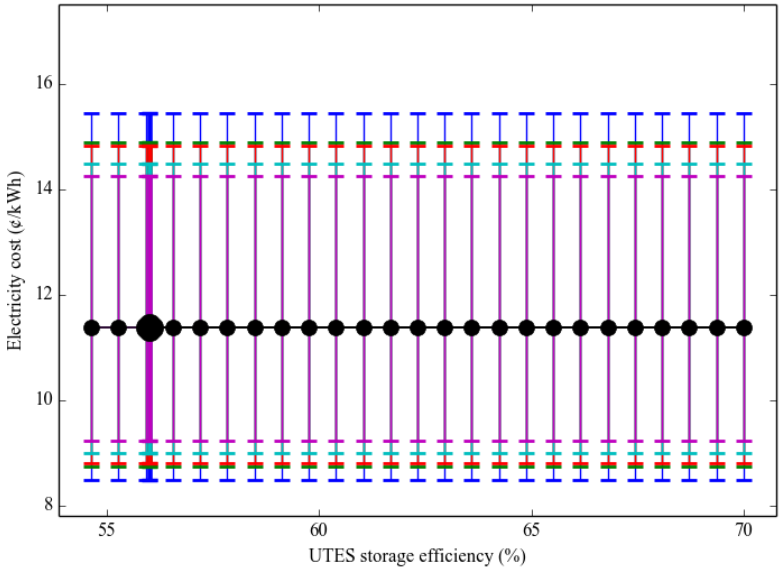

Figure S18. Same as Figure S7, but for sensitivity of the LCOE to round-trip efficiency of storage to and from phase-change materials coupled with concentrated solar power plants (PCM-CSP) (not efficiency of turbine or solar collectors). Baseline value = 99%.

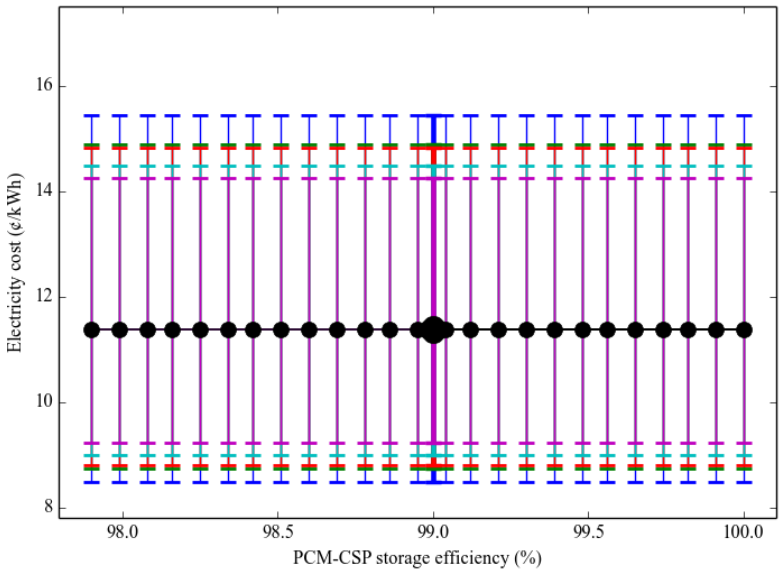

Figure S19. Same as Figure S7, but for sensitivity of the LCOE to percentage of transportation load that is flexible. Baseline value = 85%.

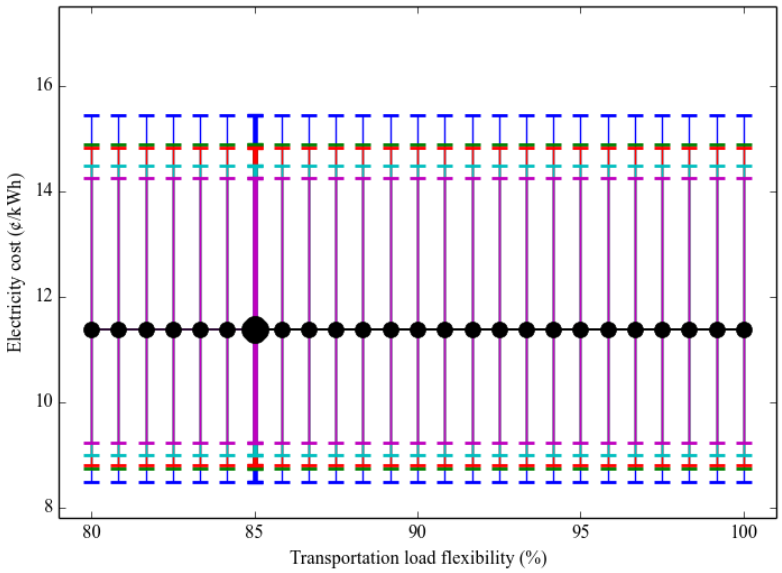

S4. Supporting References and Notes

1. Jacobson MZ (2001) GATOR-GCMM: A global- through urban- scale air pollution and weather forecast model: 1. Model design and treatment of subgrid soil, vegetation, roads, rooftops, water, sea ice, and snow. *J Geophys Res* 106(D6): 5385-5402.
2. Jacobson MZ, Archer CL (2012) Saturation wind power potential and its implications for wind energy. *Proc Natl Acad Sci USA* 109(39): 15679-15684.
3. Jacobson MZ, Archer CL, Kempton W (2014) Taming hurricanes with arrays of offshore wind turbines. *Nature Clim Chang* 4: 195-200.
4. Jacobson MZ, et al. (2015) 100% clean and renewable wind, water, and sunlight (WWS) all-sector energy roadmaps for the 50 United States. *Energy Environ Sci* 8: 2093-2117.
5. Arakawa A, Lamb VR (1981) A potential enstrophy and energy conserving scheme for the shallow water equations. *Mon Weather Rev* 109(1): 18-36.
6. Walcek CJ, Aleksic NM (1998) A simple but accurate mass conservative, peak-preserving, mixing ratio bounded advection algorithm with FORTRAN code. *Atmos Environ* 32(22): 3863-3880.
7. Jacobson MZ, Ten Hoeve JE (2012) Effects of urban surfaces and white roofs on global and regional climate. *J Clim* 25(3): 1028-1044.
8. Ketefian GS, Jacobson MZ (2009) A mass, energy, vorticity, and potential enstrophy conserving lateral fluid-land boundary scheme for the shallow water equations. *J Comput Phys* 228(1): 1-32.
9. Jacobson MZ (2005) Studying ocean acidification with conservative, stable numerical schemes for nonequilibrium air-ocean exchange and ocean equilibrium chemistry. *J Geophys Res* 110(D7): D07302, 10.1029/2004JD005220.
10. Garratt JR (1992) *The Atmospheric Boundary Layer* (Cambridge Univ. Press, Cambridge), pp 101.
11. Jacobson MZ (1998) Improvement of SMVGEAR II on vector and scalar machines through absolute error tolerance control. *Atmos Environ* 32(4): 791-796.
12. Jacobson MZ (2002) Analysis of aerosol interactions with numerical techniques for solving coagulation, nucleation, condensation, dissolution, and reversible chemistry among multiple size distributions. *J Geophys Res* 107(D19): AAC 2-1-AAC 2-23.
13. Jacobson MZ, Kaufmann YJ, Rudich Y (2007) Examining feedbacks of aerosols to urban climate with a model that treats 3-D clouds with aerosol inclusions. *J Geophys Res* 112(D24): D24205, 10.1029/2007JD008922.

14. Jacobson MZ (2012) Investigating cloud absorption effects: Global absorption properties of black carbon, tar balls, and soil dust in clouds and aerosols. *J Geophys Res* 117(D6): D06205, 10.1029/2011JD017218.
15. Jacobson MZ (2003) Development of mixed-phase clouds from multiple aerosol size distributions and the effect of the clouds on aerosol removal. *J Geophys Res* 108(D8):4245 10.1029/2002JD002691.
16. Clarke AD, Owens SR, Zhou J (2006) An ultrafine sea-salt flux from breaking waves: Implications for cloud condensation nuclei in the remote marine atmosphere. *J Geophys Res* 111(D6): D06202, 10.1029/2005JD006565.
17. Smith MH, Harrison NM (1998) The sea spray generation function. *J Aerosol Sci* 29: Suppl. 1, S189-S190.
18. Jacobson MZ, Streets DG (2009) The influence of future anthropogenic emissions on climate, natural emissions, and air quality. *J Geophys Res* 114(D8): D08118, 10.1029/2008JD011476.
19. Flanner MG, Zender CS (2006) Linking snowpack microphysics and albedo evolution. *J Geophys Res* 111(D12): D12208, 10.1029/2005JD006834.
20. Toon OB, McKay CP, Ackerman TP, Santhanam K (1989) Rapid calculation of radiative heating rates and photodissociation rates in inhomogeneous multiple scattering atmospheres. *J Geophys Res* 94(D13): 16287-16301.
21. Jacobson MZ (2005) A refined method of parameterizing absorption coefficients among multiple gases simultaneously from line-by-line data. *J Atmos Sci* 62(2): 506-517.
22. Ackerman TP, Toon OB (1981) Absorption of visible radiation in atmosphere containing mixtures of absorbing and nonabsorbing particles. *Appl Opt* 20(20): 3661-3667.
23. Kirchstetter TW, Novakov T, Hobbs PV (2004) Evidence that spectral light absorption by aerosols emitted from biomass burning and motor vehicles is different due to organic carbon. *J Geophys Res* 109(D21): D21208, 10.1029/2004JD004999.
24. Alexander DTL, Crozier PA, Anderson JR (2008) Brown carbon spheres in East Asian outflow and their optical properties. *Science* 321(5890): 833-836.
25. Chylek P, Ramaswamy V, Cheng RJ (1984) Effect of graphitic carbon on the albedo of clouds. *J Atmos Sci* 41(21): 3076-3084.
26. National Renewable Energy Laboratory (2014) Western wind dataset (NREL, Golden, CO).
27. National Renewable Energy Laboratory (2014) Eastern wind dataset (NREL, Golden, CO).
28. Mellor GL, Yamada T (1982) Development of a turbulence closure model for geophysical fluid problems. *Rev Geophys Space Phys* 20(4): 851-875.
29. Wikipedia (2014) Ivanpah solar power facility. Available at http://en.wikipedia.org/wiki/Ivanpah_Solar_Power_Facility. Accessed December 30, 2014.
30. Rehau (2011) Underground thermal energy storage. Available at http://www.igshpa.okstate.edu/membership/members_only/proceedings/2011/100611-1030-B-Christopher%20Fox%20-%20Rehau%20-%20Underground%20Thermal%20Energy%20Storage.pdf. Accessed December 27, 2014.
31. Jacobson MZ (2001) GATOR-GCMM: 2. A study of day- and nighttime ozone layers aloft, ozone in national parks, and weather during the SARMAP field campaign. *J Geophys Res* 106(D6): 5403-5420.
32. Wikipedia (2014) Availability factor. Available at http://en.wikipedia.org/wiki/Availability_factor. Accessed February 2, 2015.
33. Wikipedia (2015) Deterministic system. Available at http://en.wikipedia.org/wiki/Deterministic_system. Accessed February 12, 2015.
34. Wikipedia (2015) Stochastic. Available at http://en.wikipedia.org/wiki/Stochastic. Accessed February 12, 2015.
35. Poonpun P, Jewell WT (2008) Analysis of the cost per kilowatt hour to store electricity. *IEEE Transactions on Energy Conversion* 23(2): 529-534.
36. International Renewable Energy Agency (2013) Thermal energy storage. *IEA-ETSAP and IRENA Technology Brief E17* (IRENA, Abu Dhabi).
37. Habeebullah BA (2006) Economic feasibility of thermal energy storage systems: Application to Al-Haram Grand Holy Mosque. *JKAU: Eng. Sci.* 16(2): 55-82.
38. Nithyanandam K, Pitchumani R (2014) Cost and performance analysis of concentrating solar power systems with integrated latent thermal energy storage. *Energy* 64: 793-810.
39. Gaine K, Duffy A (2010) A life cycle cost analysis of large-scale thermal energy storage for buildings using combined heat and power. *Zero Emission Buildings Conference Proceedings*, eds Haase M, Andresen I, Hestnes A (Trondheim, Norway), 7-8 June 2010.

40. Wikipedia (2014) Pumped-storage hydroelectricity. Available at http://en.wikipedia.org/wiki/Pumped-storage_hydroelectricity. Accessed December 21, 2014.
41. Ibrahim H, Ilinca A (2013) Techno-economic analysis of different energy storage technologies. *Energy Storage - Technologies and Applications*, ed Zobaa A, 10.5772/52220.
42. Wikipedia (2014) Thermal-energy storage. Available at http://en.wikipedia.org/wiki/Thermal_energy_storage. Accessed December 21, 2014.
43. Sibbitt B, et al. (2012) The performance of a high solar fraction seasonal storage district heating system – five years of operation. *Energy Procedia* 30: 856-865.
44. Federal Energy Regulatory Commission (2014) Pumped storage projects. Available at http://www.ferc.gov/industries/hydropower/gen-info/licensing/pump-storage.asp. Accessed December 22, 2014.
45. NC Public Power (2015) Large commercial solar thermal projects. Available at http://www.ncpublicpower.com/Libraries/Solar_Energy_Studies/Large_Commercial_Case_Study.sflb.ashx. Accessed March 2, 2015.
46. International Energy Agency's Solar Heating and Cooling Programme (2004) Converting solar thermal collector area into installed capacity (m^2 to kW_{th}). Available at www.iea-shc.org. Accessed March 2, 2015.
47. Frew BA (2014) Optimizing the integration of renewable energy in the United States, Ph.D. Dissertation, Stanford University. Available at http://purl.stanford.edu/hr320qr0229.
48. Corcoran (Frew) BA, Jenkins N, Jacobson MZ (2012) Effects of aggregating electric load in the United States. *Energy Policy* 46: 399-416.